

Master in Photonics

MASTER THESIS WORK

**QUANTUM SIMULATION
OF ATTOSECOND PHYSICS**

Md Masudur Rahman

Supervised by Prof. Dr. Maciej Lewenstein, (ICFO)

Presented on date 9th September 2019

Registered at

 **Escola Tècnica Superior
d'Enginyeria de Telecomunicació de Barcelona**

Quantum Simulation of Attosecond Physics

MD MASUDUR RAHMAN^{1,2,3,*}

¹*ICFO-Institut de Ciències Fotòniques, The Barcelona Institute of Science and Technology, 08860 Castelldefels (Barcelona), Spain*

²*Universitat Politècnica de Catalunya (UPC) Barcelona Tech, 08034 Barcelona, Spain*

³*Aix Marseille Université, CNRS, Centrale Marseille, Institut Fresnel, UMR 7249, 13013 Marseille, France*

**Md-Masudur.Rahman@icfo.eu*

Abstract: We develop a numerical simulator to solve the time-dependent Schrödinger equation (TDSE) to simulate strong field ionization of a single electron under the influence of a one-dimensional separable potential. We use the split-step method to solve TDSE, obtain the ground state using the imaginary time method and benchmark it with the exact diagonalization of Hamiltonian. We perform the stability analysis in both real-time and imaginary-time propagation and obtain the fact that the usual model of separable orbital is not suitable in this method and demonstrate how a Gaussian model can solve this issue. Finally, we perform a comparative analysis between the analytical ground state and an adapted version of ground state adjusted according to the time-step of TDSE to justify the origin of the numerical error.

This master's thesis was written under the supervision of Prof. Dr. Maciej Lewenstein, and Dr. Emilio Pisanty. It is presented to opt for the title of Master in Photonics, Europhotonics.

Date: 31 August 2019

1. Introduction

Strong field ionization (SFI) [1, 2] is a highly nonlinear process where interesting quantum phenomena comes into play, because the strong laser field being comparable to the internal binding potential of atom breaks the perturbative approximation. There are different types of SFI, namely multiphoton ionization [3, 4], tunneling ionization [5], single electron ionization and multiple electron ionization. In case of double electron ionization, two electrons can be ionized either sequentially (without the help of the first ionized electron) or non-sequentially (with the impact of the first ionized electron). The latter is known as nonsequential double ionization (NSDI), in which the ionized electrons are known to be classically correlated. [5-8]. However, questions remain about the quantum nature of those correlations, such as the presence of entanglement and nonlocality [9, 10], as well as about the full characterization of the quantum state in single ionization.

Multiple tools, both numerical and analytical, have been used, with the Strong-Field Approximation forming the workhorse method for analytical work [2]. One specific tool that has been useful for analytical treatments has been separable potentials [11-15; for a review see 1], since rank-one separable potentials can be used to model quantum systems which have only one bound state, as used in the Strong-Field Approximation. Nevertheless, separable potentials remain relatively unexplored within numerical frameworks.

In this contribution, we develop numerical simulations to solve the time-dependent Schrödinger equation (TDSE) for single-electron strong-field ionization in the case of a separable potential of the form $\hat{V} = -\gamma|\phi\rangle\langle\phi|$, with a view to analyzing the quantum state of a single electron and, eventually, the quantum nature of correlations in NSDI. Our approach is based on the split-step method to propagate the TDSE, as well as the imaginary-time method to find the ground state. We benchmark the ground state against the exact diagonalization of the Hamiltonian. Our results from the imaginary-time method show that the usual inverse-square-root-based separable potential is not suitable for the split-step method. As a solution, we propose a Gaussian model for which the imaginary-time method does converge satisfactorily to the ground state, and we demonstrate analytically the reason of this

convergence. We analyze the convergence criteria in the case of real-time propagation of the TDSE, and our results confirm that the accuracy suffers from round-off error. In addition, we demonstrate the effects of time-discretization errors in real-time propagation by constructing adapted versions of the ground state for the different propagation schemes. Finally, we suggest some possible solutions to the remaining numerical inaccuracies, to be implemented as future work.

2. An overview of Strong Field Ionization

The ionization regime can be identified by the Keldysh parameter $\gamma = \sqrt{I_p/2U_p}$, where I_p is the ionization potential and U_p is the ponderomotive energy, that is, the average kinetic energy of the oscillations of a free electron in a laser field, which depends both on the intensity and wavelength of light as $U_p \propto I_0 \lambda_0^2$. If the laser frequency ω is high (i.e. λ_0 is short), $\hbar\omega > I_p$, one single photon can ionize the atom, and a strong field is not required. However, if the laser frequency is low enough to consider $\hbar\omega < I_p$ and the field is intense enough, multi-photon ionization can occur. For short intense pulses, the continuum energy gets shifted by U_p and the kinetic energy of the emitted electron becomes $n\hbar\omega - I_p - U_p$ where n is the number of photons absorbed by the electron. The value of U_p can be varied by tuning the intensity I_0 of the laser field. In the multiphoton ionization regime, where ponderomotive energy is smaller than the ionization potential, $\gamma > 1$.

There is an extension of multi-photon ionization called above-threshold ionization (ATI) [11-13, 16] where multiple photons are absorbed to not only access the ionization continuum but to surpass the I_p by more than one photon. ATI will be observed if $n > n_{min}$, where n_{min} is the minimum number of absorbed photons required for ionization. Hence, the kinetic energy of the electron in case of multiphoton ionization has the expression $(n_{min} + n_{ext})\hbar\omega - I_p$ where $n_{ext} = 0, 1, 2, \dots$ and we observe spectra with peaks separated by $\hbar\omega$.

If the intensity is increased in such a way that U_p exceeds I_p , making $\gamma < 1$, we are no longer in the multiphoton ionization regime. Rather, the high value of electric field distorts the Coulomb potential, and tunneling ionization takes place. In this case, the intense electric field distorts the potential barrier of an atom or molecule drastically. Therefore, the height of the barrier that electrons must pass decreases and electrons can escape from the potential more easily. If we increase the intensity even more such that $\gamma \ll 1$, we get over-the-barrier ionization regime.

We know that atomic potentials commute in position space but do not commute in momentum space. It is obviously interesting to investigate the SFI in the general case where $[\hat{V}, \hat{p}] \neq 0$ and $[\hat{V}, \hat{x}] \neq 0$ which we can find in case of the separable potentials.

3. Methods

In order to solve the time-dependent Schrödinger equation (TDSE), we have used the split-step method, which is basically a pseudo-spectral differential equation solver i.e. it solves the time-dependent Schrödinger equation with Fourier transformation [17-20].

3.1 The Split-step method

The time evolution of the wavefunction of an electron under the influence of a one-dimensional potential is governed by the Schrödinger equation,

$$i\hbar \frac{\partial}{\partial t} \psi(x, t) = \left[-\frac{\hbar^2}{2m} \frac{\partial^2}{\partial x^2} + \hat{V} \right] \psi(x, t), \quad (1)$$

where m is the mass of electron, \hbar is the Planck constant and $\psi(x, t)$ is the wavefunction at time t and position x . In the Hamiltonian shown above, \hat{V} is the potential energy operator and $-(\hbar^2/2m) \partial^2/\partial x^2$ is the kinetic energy operator that will be denoted with \hat{K} later. If we consider simulating our system by a series of small timesteps (Δt), after each time-step we get the time-evolved solution, based on the wave-function obtained in the last step, which can be described in the following way,

$$\psi(r, t + \Delta t) = e^{-\frac{i}{\hbar}(\hat{K} + \hat{V})\Delta t} \psi(r, t), \quad (2)$$

where the time-ordering operator is dropped considering small value of Δt . At this point, we can perform a splitting in the operator by using the Baker-Campbell-Hausdorff-Dynkin formula [21]:

$$\psi(r, t + \Delta t) = e^{-\frac{i}{\hbar}\hat{K}\Delta t} e^{-\frac{i}{\hbar}\hat{V}\Delta t} e^{-\frac{i}{\hbar}[\hat{K}, \hat{V}]\Delta t^2} \psi(r, t) = e^{-\frac{i}{\hbar}\hat{K}\Delta t} e^{-\frac{i}{\hbar}\hat{V}\Delta t} \psi(r, t) + O(\Delta t^2), \quad (3)$$

This accrues a small amount of error (Δt^2) related to the commutation of the kinetic and potential parts of the Hamiltonian. We can further minimize the error from the order of Δt^2 to the order of Δt^3 through the splitting of the system i.e. by performing a half-step in one operator before doing a full step in the other operator,

$$\psi(r, t + \Delta t) = e^{-\frac{i}{\hbar 2}\hat{K}\Delta t} e^{-\frac{i}{\hbar}\hat{V}\Delta t} e^{-\frac{i}{\hbar 2}\hat{K}\Delta t} \psi(r, t) + O(\Delta t^3), \quad (4)$$

in a process called Strang splitting [22].

The fact that \hat{K} has simpler expression $\hat{p}^2/2m$ in momentum space and, that the atomic potential \hat{V} is usually expressed in position space, it is much simpler to work in momentum space with $\exp(-i\hat{K}\Delta t/\hbar)$ and in position space with $\exp(-i\hat{V}\Delta t/\hbar)$, because it facilitates us to work with diagonal matrices. We can address each part of this solution segment-wise: first in momentum space, then in position space, then back in momentum space, by using Fourier Transforms to switch between domains. This can be expressed mathematically in the form,

$$\psi(r, t + \Delta t) = F^{-1} \left[e^{-\frac{i}{\hbar 2}\hat{K}\Delta t} F \left[e^{-\frac{i}{\hbar}\hat{V}\Delta t} F^{-1} \left[e^{-\frac{i}{\hbar 2}\hat{K}\Delta t} F[\psi(r, t)] \right] \right] \right] + O(\Delta t^3), \quad (5)$$

where F and F^{-1} indicate forward and inverse Fourier Transforms.

In absence of laser field, we do not need to use back and forth Fourier operation in our simulation because the orbital of separable potential can be modeled in momentum space that makes it convenient to calculate the time evolution in one single space as follows:

$$\psi(p, t + \Delta t) = e^{-\frac{i}{\hbar 2}\hat{K}\Delta t} e^{-\frac{i}{\hbar}\hat{V}\Delta t} e^{-\frac{i}{\hbar 2}\hat{K}\Delta t} \psi(p, t) + O(\Delta t^3). \quad (6)$$

In Eq.6, the potential operator $\exp(-i\hat{V}\Delta t/\hbar)$ can be significantly simplified by expanding into Taylor series and using $\langle \phi | \phi \rangle = 1$ as follows:

$$\begin{aligned} e^{-\frac{i}{\hbar}\hat{V}\Delta t} &= \sum_{n=0}^{\infty} \frac{1}{n!} \left(\frac{i}{\hbar} \gamma \Delta t |\phi\rangle\langle\phi| \right)^n = \mathbb{I} + |\phi\rangle\langle\phi| \sum_{n=1}^{\infty} \frac{1}{n!} \left(\frac{i}{\hbar} \gamma \Delta t \right)^n \\ &= \mathbb{I} + \left(e^{\frac{i}{\hbar}\gamma \Delta t} - 1 \right) |\phi\rangle\langle\phi| \end{aligned} \quad (7)$$

In the previous discussions, we did not consider any laser field. The presence of laser field $F(t)$ adds a separate interaction term \hat{U} to the Hamiltonian \hat{H} and makes it time-dependent i.e. $\hat{H}(t) = \hat{K} + \hat{V} + \hat{U}(t)$, where $\hat{U}(t) = \hat{x} F(t)$ in length gauge. The field has the expression: $F(t) = F_0 \sin^2(\omega t/2N_c) \cos \omega t$, where ω and F_0 are the frequency and the maximum value of the electric field respectively, and N_c is the number of optical cycles in each laser pulse, and $F_0 \sin^2(\omega t/2N_c)$ is the pulse envelope. As it is convenient to operate with $\exp(-i\hat{U}\Delta t/\hbar)$ in position space, we need to transform the wavefunction obtained from Eq. 6 into position space at first. After the laser operation is over, we need to transform the wavefunction back into momentum space to use Eq. 6 again.

3.2 Other possible methods to solve TDSE

The split-step method described earlier is one of the many methods to solve TDSE. Among the other possible methods, Runge-Kutta method, Krylov sub-space method and Crank-Nicolson method can be mentioned [23]. The Runge-Kutta method is a way to solve coupled partial differential equations. In the explicit version of the Runge-Kutta method, the solution is a linear combination of some vectors, if the Hamiltonian is considered time-independent. On the contrary, the implicit method requires the solution of a usually large linear system of equations. The Krylov subspace method is basically a polynomial approximation which has similarity with the explicit Runge-Kutta method. Crank-Nicolson method is an implicit method but gives better accuracy compared to the implicit Runge-Kutta method.

3.3 Imaginary Time method to find the ground state

The same TDSE code can be used to obtain the ground state by using imaginary time [24]. TDSE (Eq. 1) can be written by expanding the initial state $\psi(r, 0)$ in the basis of the solutions of time independent Schrödinger equation,

$$\left[-\frac{\hbar^2}{2m} \nabla^2 + \hat{V} \right] \psi_n(r) = E_n \psi_n(r), \quad (8)$$

and multiplying each term in the expansion by a complex-valued time-dependent phase factor:

$$\psi(r, t) = \sum_{n=0}^{\infty} c_n e^{-\frac{i}{\hbar} E_n t} \psi_n(r), \quad (9)$$

where E_n is the eigenenergy. Now, replacing the variable t with an imaginary time variable $t = -i\tau$, we obtain:

$$\psi(r, \tau) = c_0 e^{-\frac{1}{\hbar} E_0 \tau} \psi_0(r) + \sum_{n>0} c_n e^{-\frac{1}{\hbar} E_n \tau} \psi_n(r). \quad (10)$$

The ground state has the minimum energy among all the states i.e. $E_0 < E_n$ for $n > 0$. Therefore, in case of large τ , the first term associated to ground state will be much dominant compared to the rest of the terms. So, in the limit of large τ , the wave function is,

$$\psi(r, \tau) \approx c_0 e^{-\frac{1}{\hbar} E_0 \tau} \psi_0(r) \quad (11)$$

i.e. after normalization, it is approximately the same as the ground state $\psi_0(r)$. We can also calculate the energy of ground state by considering $\psi(r, \tau + \Delta\tau)$ as follows:

$$E_0 \approx -\frac{\hbar}{\Delta\tau} [\ln \psi(r, \tau + \Delta\tau) - \ln \psi(r, \tau)], \quad (12)$$

where τ is a large number. In imaginary time evolution, the norm of the wavefunction is not preserved. So, one needs to normalize the wavefunction in each TDSE step to prevent the norm from changing in an exponential way.

3.4 Implementation

If we discretize both spaces with N number of points, the resolution in momentum and position space is $\Delta p = P_0/(N - 1)$ and $\Delta x = X_0/(N - 1)$ respectively, where, P_0 and X_0 are the range of momentum and position under calculation. The Fourier relation between two spaces being $P_0 = 2\pi/\Delta x$ gives the following expression connecting P_0 , X_0 and N .

$$X_0 P_0 = 2\pi(N - 1) \quad (13)$$

The number of points is taken in the format of 2^n , where n is a positive integer, so that fast Fourier transform (FFT) can be applicable. From now on, we use all the values in atomic units unless specified where $m = 1$, $\hbar = 1$, $e = 1$ and $4\pi\epsilon_0 = 1$ are considered.

Our implementation of the TDSE code in MATLAB can be run both on desktop computers and, if higher speed and throughput is required on the ICFO computing cluster. Our implementation has been archived as [25].

4. Results and Discussion

4.1 Comparison to the exact diagonalization of Hamiltonian

In this section, we compare the analytical expression of ground state with the one obtained with exact diagonalization. The ground state $|\psi_0\rangle$ of separable potential has the following expression in the momentum representation [2, 13]:

$$\psi_0(p) = \frac{N \phi(p)}{\frac{1}{2}p^2 + I_p}, \quad (14)$$

where $\phi(p) = \langle p|\phi\rangle$ is the momentum-space representation of $|\phi\rangle$, N is the normalization constant, I_p is the ionization potential, p represents the momentum and m is the mass of electron. The expression of the coupling constant γ is derived in the Appendix section A1.1. Here, we use the model [26]:

$$\phi(p) = N/\sqrt{p^2 + \Gamma^2}, \quad (15)$$

where N is a normalization constant and Γ is a potential softening parameter.

The elements of Hamiltonian matrix in momentum space is as follows:

$$\langle p_i|\hat{H}|p_j\rangle = \frac{1}{2}p_i^2 \delta_{ij} - \gamma \phi^*(p_i)\phi(p_j). \quad (16)$$

After diagonalizing the Hamiltonian, we obtain the eigenvalues and corresponding eigenfunctions. The eigenfunction associated to the minimum energy eigenvalue is the ground state wave function. In case of separable potential of rank one, there is only one bound state i.e. it has only one negative eigenvalue, and the bound state is the ground state $|\psi_0\rangle$ with the energy $\langle\psi_0|\hat{H}|\psi_0\rangle$. In Fig.1 we plot the ground state in momentum space obtained from the exact diagonalization of the Hamiltonian (in red) and we compare it with the one obtained analytically (in blue) from Eq. 14.

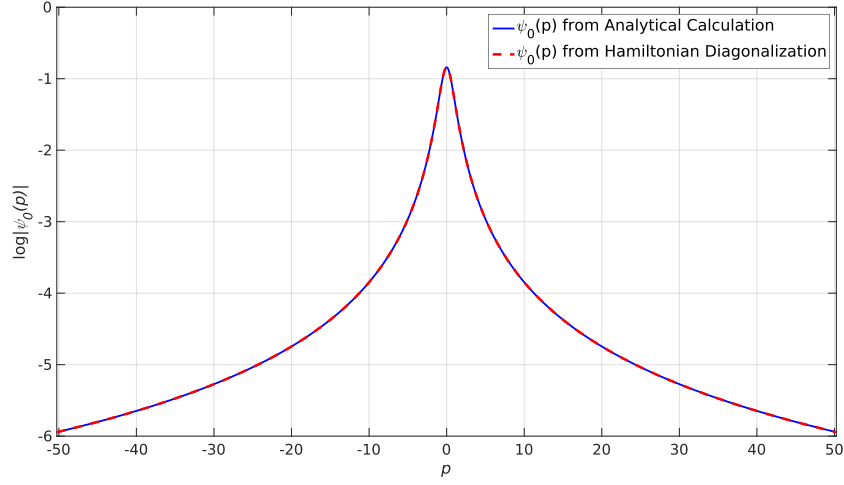


Fig. 1. $\log|\psi_0(p)|$ versus momentum p is shown here in this graph. The blue line corresponds to the ground state obtained from the exact diagonalization of Hamiltonian, while the red dashed line represents the ground state wavefunction in logarithmic scale calculated using analytical expression.

4.2 Finding the ground state using the Imaginary Time method

The imaginary-time method does not converge numerically at large momentum regions in the case of separable potential modeled with Eq. 15, which is demonstrated in Fig.2.

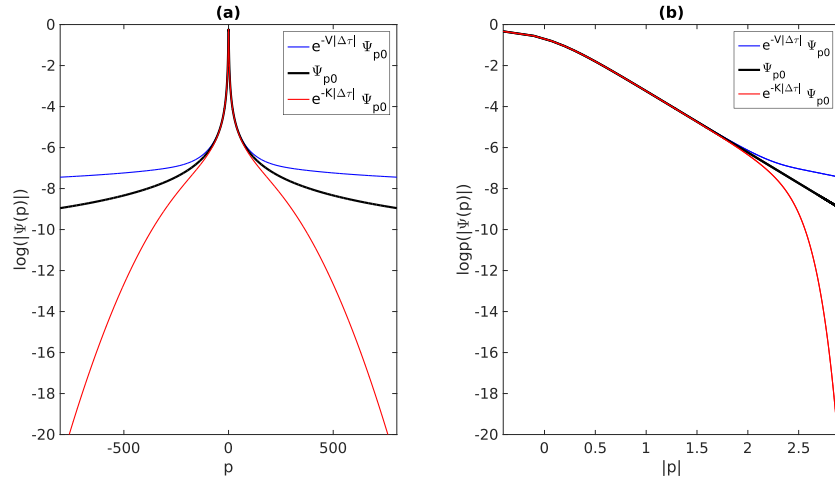


Fig. 2. Failure of convergence in the large momentum region in case of $\phi = N/\sqrt{p^2 + \Gamma^2}$. Here, the analytical ground state is given as the initial state of imaginary-time TDSE simulation. As the wavefunction becomes extremely small at the high momentum region, log-lin. scale (left graph) and log-log scale (right graph) is shown to exhibit the precise details.

From Eq. 14 and Eq. 15, we find that at large momentum (i.e. $|p| \gg \Gamma, \sqrt{2I_p}$), the ground state and its expression after operating with the potential and the kinetic operator becomes:

$$\psi_0 \approx 2N/p^3 \sim p^{-3} \quad (17)$$

$$e^{-\hat{V}|\Delta\tau|}\psi_0 \approx \left(\frac{2}{p^2} + |\Delta\tau|\right) \frac{N}{p} \sim p^{-1} \quad (18)$$

$$e^{-\hat{K}|\Delta\tau|}\psi_0 \approx e^{-\frac{p^2}{2m}|\Delta\tau|} \frac{2N}{p^3} \sim e^{-\frac{p^2}{2m}|\Delta\tau|} p^{-3}, \quad (19)$$

respectively. From Eq.18 and Eq.19, we see that the potential and kinetic operator acting on ψ_0 makes the state converge to ψ_0 , if the following condition:

$$|p| \ll \sqrt{2/|\Delta\tau|}, \quad (20)$$

on momentum is true. This is the reason why the convergence towards ground state starts to fail for large momentum as shown in Fig. 2. Although the convergence of norm is obtained as the population is mostly occupied in the low momenta region, we need convergence in large momenta regime as well. Therefore, we conclude that this model of separable potential with orbital given in Eq. 15 is not a suitable choice to use in split-step method of TDSE.

We consider a Gaussian model of the orbital,

$$\phi(p) = N \exp(-p^2/\Gamma^2), \quad (21)$$

and show that the ground state converges satisfactorily even at large momenta regime. A comparison of these two models is shown graphically in the Appendix Section A2.

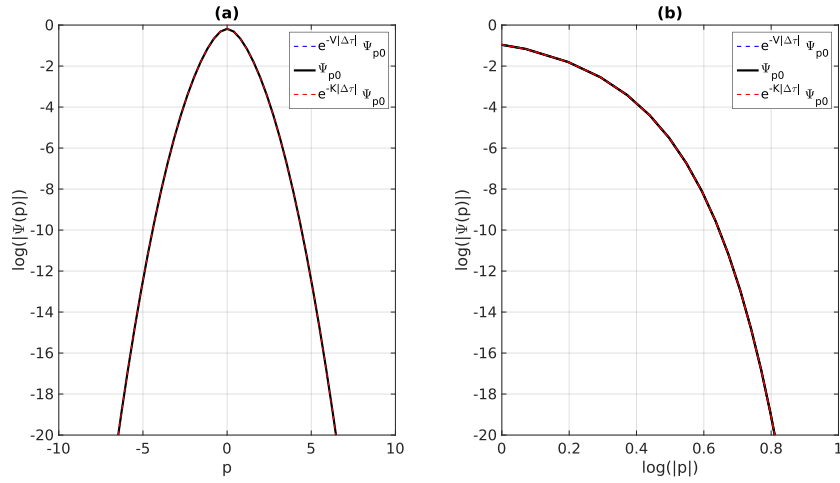


Fig. 3. Convergence characteristics in case of $\phi = N e^{-p^2/\Gamma^2}$ with $\Gamma = 1$. Here, the ground state wavefunction (represented in black continuous line) remains almost the same after operating with the kinetic operator (represented in red dashed line) and potential operator (represented in blue dashed line).

The reason of this convergence can be understood by seeing the Eqs. 22-24 as compared to the Eqs. 17-19. In the case of Gaussian model,

$$\psi_0 \approx -(2/\Gamma^2) N e^{-p^2/\Gamma^2} \sim e^{-p^2/\Gamma^2} \quad (22)$$

$$e^{-\hat{V}|\Delta\tau|}\psi_0 \approx \left(-\frac{2}{\Gamma^2} + |\Delta\tau|\right) N e^{-p^2/\Gamma^2} \sim e^{-p^2/\Gamma^2} \quad (23)$$

$$e^{-\hat{K}|\Delta\tau|}\psi_0 \approx -\frac{2}{\Gamma^2} N e^{-p^2\left(\frac{1}{\Gamma^2} + \frac{|\Delta\tau|}{2}\right)} \sim e^{-p^2\left(\frac{1}{\Gamma^2} + \frac{|\Delta\tau|}{2}\right)}, \quad (24)$$

which give the following condition of convergence:

$$|\Delta\tau| \ll 2/\Gamma^2. \quad (25)$$

The fact that the momentum term is absent in the condition of Eq. 25, while it was present in Eq. 20, facilitates the convergence characteristics in this case. A comparison between these two models are given in the Annex section A2.1.

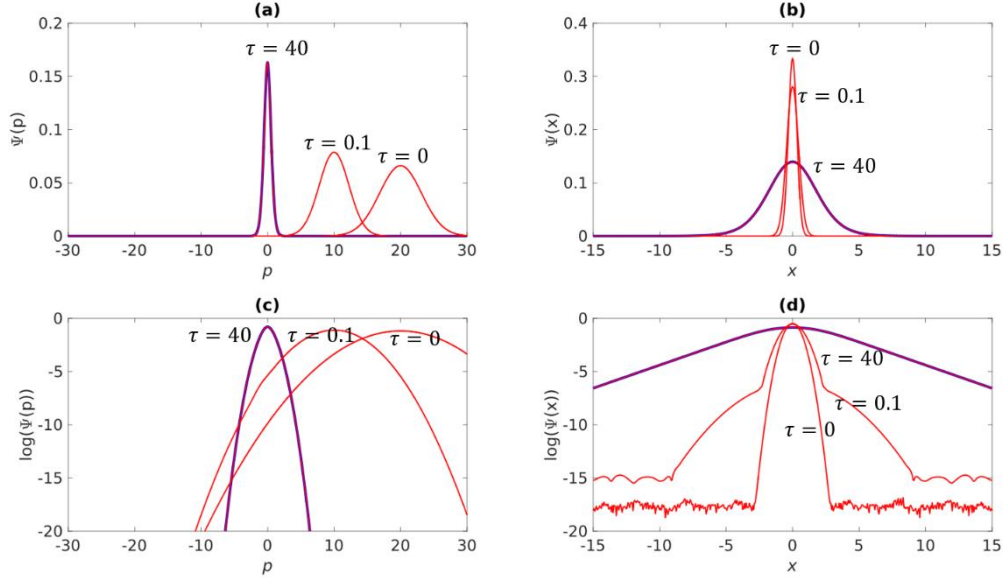


Fig. 4. Convergence of an arbitrary state to the ground state of separable potential using the imaginary time method. In the simulation all the values are considered in atomic unit. The blue colored curve is the ground state calculated analytically and a shifted Gaussian is chosen as the arbitrary state (red curve at $\tau = 0$). The time evolved states at $\tau = 0.1$ and $\tau = 40$ are shown in both momentum space (left ones) and position space (right ones).

In Fig. 4 we demonstrate how the imaginary-time method makes an arbitrary initial state converge towards the ground state of the separable potential of orbital $\phi(p) = N \exp(-p^2/\Gamma^2)$ with $\Gamma = 1$. We use a Gaussian state of the form $N e^{-b(p-c)^2}$ as an initial state, where N is a normalization constant, b and c are the width-setting and center-locating parameters, respectively. In the simulation, we use $b = 0.05$, $c = 20$, $\Delta\tau = 10^{-4}$, position window-size $X_0 = 2^8$, and the number of points $N = 2^{12}$. The window size in momentum space is automatically set as $P_0 = 2\pi(N-1)/X_0$. From Fig. 4 we observe that the given state changes both its position and shape with the passage of time in order to have the position and shape of the ground state. We can characterize the convergence of an arbitrary state to the ground state by plotting the component orthogonal to the ground state i.e. $|\psi_\perp(\tau)\rangle$ expresses as,

$$|\psi_\perp(\tau)\rangle = |\psi(\tau)\rangle - \langle\psi_0|\psi(\tau)\rangle |\psi_0\rangle. \quad (26)$$

Here, the norm of $|\psi_\perp(\tau)\rangle$ can be treated as the convergence error. This error is plotted both in linear scale and logarithmic scale in Fig. 5 for different times of TDSE simulation. We clearly see the error going down with the propagation of time.

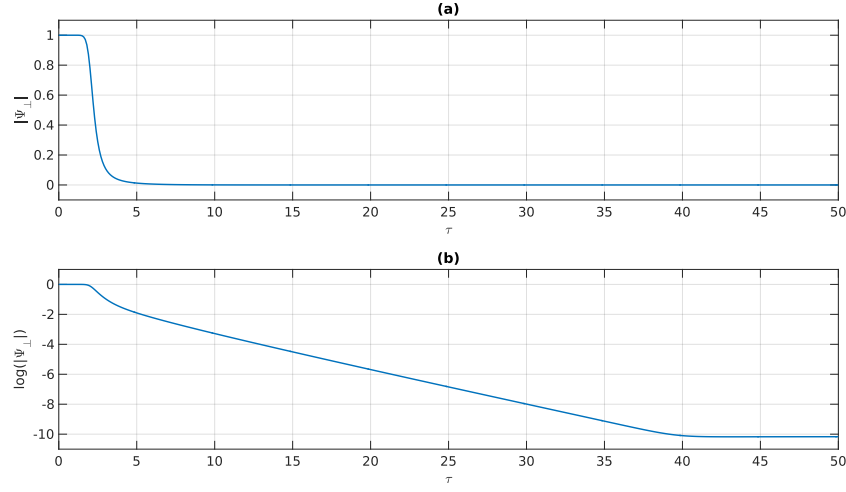


Fig. 5. The magnitude of the component of $\psi(\tau)$ orthogonal to the ground state as a function of τ . Initially the norm of the orthogonal component is unity, and with the passage of time it decreases to zero as $\psi(\tau)$ changes to get aligned with the ground state. $|\psi_{\perp}(\tau)|$ is represented both in linear scale (Fig. a) and logarithmic scale (Fig. b).

4.3 Real time TDSE

In this section, we observe how stable the ground state remain under the imaginary-time propagation. We insert the ground state of the separable potential as express in Eq. 14 as an initial state of the TDSE code in real-time propagation. The derivation of Eq. 14 is provided in the Appendix section A1.1. In principle, the state being the ground state should remain unchanged. However, we observe that it changes at the tails because of numerical problem.

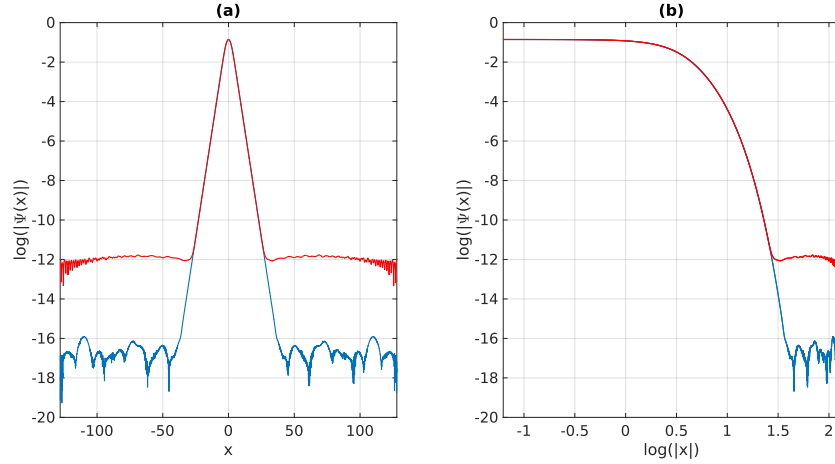


Fig. 6. The comparison of the initial state and the stable state after real-time TDSE simulation is demonstrated here. In Fig.(a), logarithmic scale is used in wave-function to observe the precise details at its low value region while in Fig.(b), the log-scale in position enables the details in lower values of position. In both figures, the blue curve corresponds to the ground state obtained analytically which is given as the initial state. With the passage of time, the wavefunction changes at tails. The red curve is the steady state obtained from TDSE simulation run with $\Delta t = 10^{-5}$. From the graphs of the wavefunction in position space, we see a clear noise in the tail region. These graphs are taken after 70 atomic unit time of propagation.

In order to characterize this numerical error, we derive (cf. Appendix section A1.2) the adjusted ground state which is compatible with the TDSE time-step Δt , which is given as follows:

$$\psi_0(p) = \frac{N e^{+i \frac{p^2}{4} \Delta t}}{1 - e^{i(I_p + \frac{p^2}{2}) \Delta t}} \phi(p). \quad (27)$$

In the Appendix sections A1.1 and A1.2, the change of the coupling constant γ is demonstrated analytically.

This expression given in Eq. 27 corresponds to the operator sequence : $e^{-\frac{i\hat{R}}{\hbar 2} \Delta t} e^{-\frac{i\hat{p}}{\hbar} \Delta t} e^{-\frac{i\hat{R}}{\hbar 2} \Delta t}$ and it converges to Eq. 14 in the limit $\Delta t \rightarrow 0$. From the expression of Eq. 27 we clearly see a constraint:

$$p < \sqrt{2(2\pi/\Delta t - I_p)}, \quad (28)$$

which means that the phase of the exponential term in the denominator must not be greater than 2π . It is even better to keep the phase $(I_p + p^2/2) \Delta t$ less than $\pi/2$ by appropriately choosing the time-step and the momentum range. With this adjusted ground state, there is no significant noise at the tail region which is shown in Fig.7, as we already introduce the discretized error in Eq. 27.

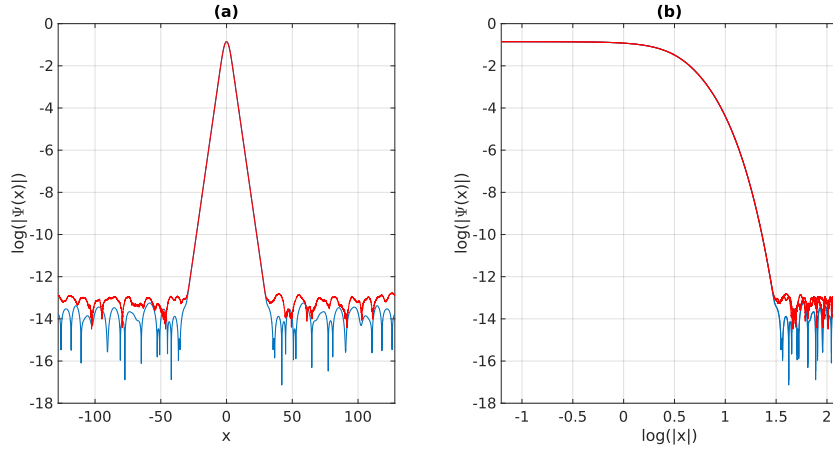


Fig. 7. Initial and final steady state in case of adjusted ground state is shown in position space. The change in state after real-time TDSE being much smaller than that obtained in Fig.8, is a clear indication of discretization error. These graphs are taken after 70 atomic unit time of propagation.

Although the adjusted ground state remains much more stable in real-time TDSE simulation than the original ground state, the final steady state in both cases (cf. the red curves of Fig. 6 and Fig. 7) are almost similar. We get an intuition from Fig.6 and Fig.7 that, the numerical noise in real-time TDSE simulation changes the original ground state to an state which is close to the adjusted ground state. Therefore, we can conclude that, the noise observed in Fig. 6 mostly comes from the discretization error.

To characterize the noise at tails, we calculate the norm of the orthogonal component $|\psi_{\perp}(p)|$ and $|\psi_{\perp}(k)|$, respectively. We run the simulation to understand the behavior of this noise level for different time-steps. The calculations are done for the analytical ground state as well as Δt -adjusted version of it, and the results are plotted in Fig. 8.

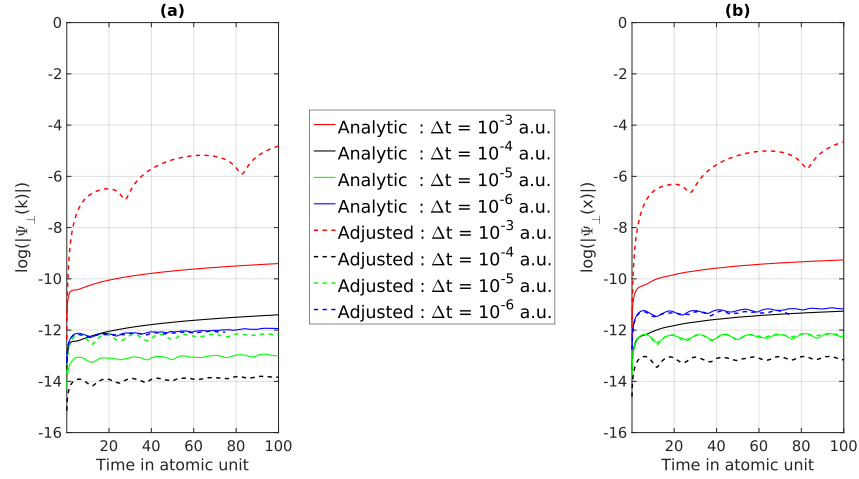


Fig. 8. The component of wave-function orthogonal to the ground state is demonstrated at different times of TDSE simulation. In Fig.(a) $\log|\psi_{\perp}(k)|$ and in Fig.(b) $\log|\psi_{\perp}(x)|$ is plotted at different TDSE times t starting from 0 to 100 atomic unit. In both graphs, continuous lines correspond to the simulations where analytical expression of ground state is used while the dashed lines are associated to the simulations with adjusted ground states.

Observing the continuous lines in both Fig. 8(a) and Fig. 8(b) we find that the decrease of time-step improves the steady state. The decrease of time-step as: $\Delta t = 10^{-3}$ (indicated in red), 10^{-4} (indicated in black) and 10^{-5} (indicated in green) gives the levels of $|\psi_{\perp}(t)\rangle$ in steady state (for t very large) closer to zero. This is expected because if $\Delta t \rightarrow 0$, so does the norm of orthogonal component i.e. $|\psi_{\perp}| \rightarrow 0$. However, we observe that $\Delta t = 10^{-6}$ (indicated in blue) deviates from this trend, which is perhaps the limitation of numerical precision used by the simulator. Moreover, for $\Delta t = 10^{-5}$ a.u. and $\Delta t = 10^{-6}$ a.u. some oscillatory behavior is observed while $\Delta t = 10^{-3}$ a.u. and $\Delta t = 10^{-4}$ a.u. provides monotonic change. The red-dotted curve corresponding to $\Delta t = 10^{-3}$ violates the condition given in Eq. 28. We are not sure about the origin of the oscillatory behavior at some curves.

The error characterized with $|\psi_{\perp}|$ is plotted up to a greater larger range for analytical and adapted ground state in Fig. 9 and Fig. 10, respectively. An increase in the error is observed in Fig. 9 if Strang splitting is not used, which is expected. However, in the case of an adapted ground state, the error is almost same both with and without the use of Strang splitting of operator the reason of which is not clear yet. Moreover, in Fig. 9 we observe a clear saturation of $|\psi_{\perp}|$, but it keeps growing in Fig. 10.

The error depends not only on the time resolution Δt but also on the resolution in space variables Δx and Δp . The error associated to these three variables is demonstrated in Fig. 11. The red colored continuous line corresponds to $N = 2^{12}$, $X_0 = 256$ and the associated value of $P_0 \approx 101$. An increase of P_0 decreases the error as shown with black colored line and vice versa is also true which is shown with blue line. Then, we changed N from 2^{12} to 2^{11} and 2^{13} which is shown with broken line and dotted line, respectively. In each case, we changed either of the X_0 and P_0 fixed or changing both simultaneously.

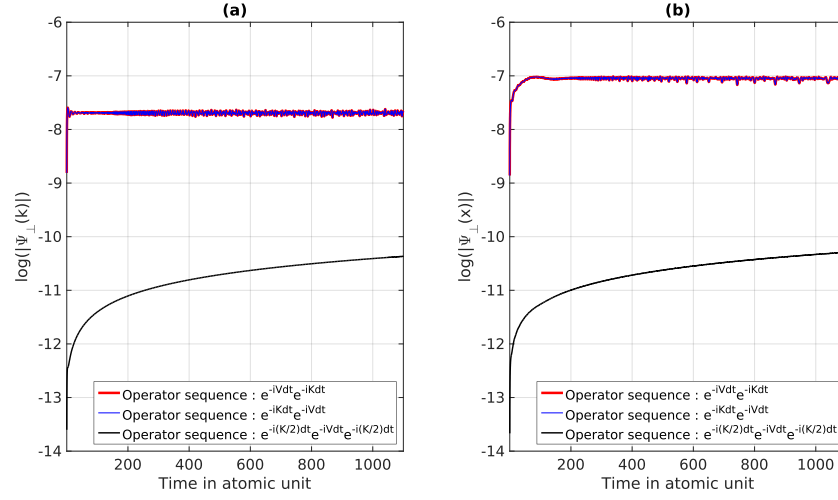


Fig. 9. Accumulation of numerical error is demonstrated up to 1100 atomic unit time for analytic ground state expressed in Eq. 14. In Fig.(a), the norm of $|\psi_{\perp}(t)\rangle$ is demonstrated in momentum space representation, and in Fig.(b) it is in position space representation, with the time-difference $\Delta t = 10^{-4}$ atomic unit in both graphs. The error property is same for both sequence of operators : $\exp(-i\hat{V}\Delta t)\exp(-i\hat{K}\Delta t)$ and $\exp(-i\hat{K}\Delta t)\exp(-i\hat{V}\Delta t)$ indicated in red and blue colors, respectively. There is a clear improvement of error in case of Strang splitting of kinetic operator which is demonstrated in black color. The time-step $\Delta t = 10^{-4}$ is used in this simulation.

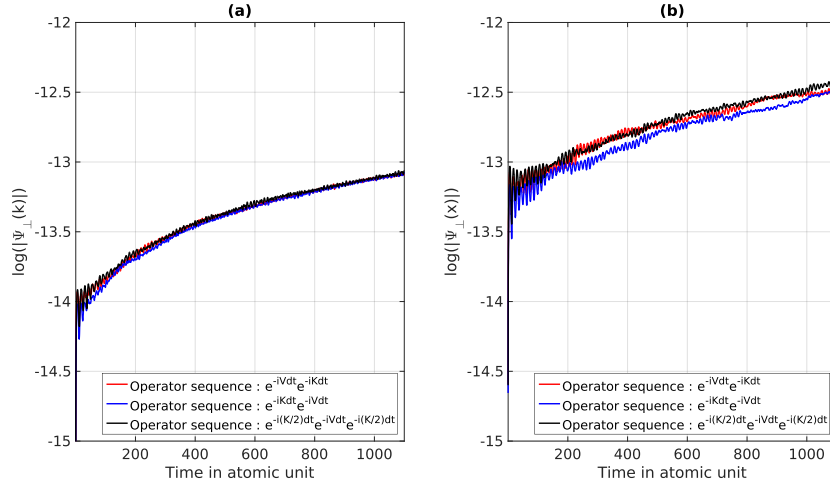


Fig. 10. Accumulation of numerical error is demonstrated up to 1100 atomic unit time for adapted ground state expressed in Eq. 27. The parameters are exactly same as in Fig. 9 except the fact that adapted ground state is used as the initial state instead of the analytically obtain ground state.

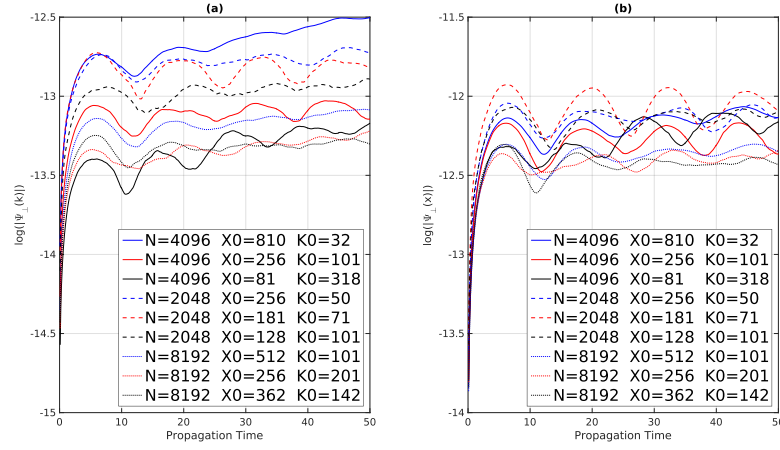


Fig. 11. Effect of different parameters: number of sampling points N as well as the window-size P_0 and X_0 in momentum space and position space, respectively is shown in this figure. In Fig.(a) the norm of $\psi_{\perp}(k)$ and in Fig.(b) the norm of $\psi_{\perp}(x)$ is plotted in log-scale at different times of TDSE propagation. The continuous lines correspond to $N = 2^{12} = 4096$, the broken lines are associated to $N = 2^{11} = 2048$ and the dotted lines indicate the data for $N = 2^{13} = 8192$. In each case (for a fixed N), three set of values of P_0 and X_0 are used. The blue line and black line are used to indicate the data for the lowest and highest value of P_0 and red line for the value of P_0 in between these two values.

From Fig. 11 we can conclude that larger number of points gives better accuracy. Moreover, an increase of window size in either space improves the accuracy in the corresponding space. In all calculations round-off error persists which might be the prime reason for unusual noise characteristics.

5. Conclusion

In this work we present, thus, the initial stages of a workable numerical code of TDSE in order to simulate strong field ionization. In this regard, while the convergence of the wavefunction of the ground state in norm is acceptable, we also require good qualitative convergence over all regions of momentum space, which presents unexpected difficulties. We find that the usual inverse-square-root model is not a suitable choice in case of the split-step method. Changing the focus on a Gaussian orbital for a separable potential yields a better qualitative convergence for the imaginary-time method without impacting the physics being simulated. From stability analysis we find that the convergence characteristic is not satisfactory mostly because of round-off error as well as from discretization error. Without mitigating the noise level in the simulation, performing the simulation in presence of a laser field will not give accurate results. To mitigate this problem there may be several options to consider as future works. One possible option is to switch to quadrupole precision, though that may require software changes as the software support is more limited. Another possible option could be the use of other methods. Finally, it is possible that the numerical noise can be mitigated by transforming the problem to the velocity gauge, where the laser coupling uses only the momentum operator, eliminating the need for Fourier transforms and their associated sources of numerical noise.

References

1. M. Y. Ivanov, M. Spanner, and O. Smirnova, "Anatomy of strong field ionization," *J. Mod. Opt.*, **52**(2-3), 165-184 (2005).
2. K. Amini *et al.*, "Symphony on Strong Field Approximation," [arXiv:1812.11447](https://arxiv.org/abs/1812.11447) (2019). *Rep. Prog. Phys.*
3. J.Z.Kaminski, "On exactly soluble models for multiphoton processes," *Czech. J. Phys.* **39**(10), 1061-1065 (1989).

4. T. Radozycki, and F. H. M. Faisal, "Multiphoton ejection of strongly bound relativistic electrons in very intense laser fields," *Phys. Rev. A* **48**(3), 2407–2412 (1993).
5. W. Becker, X. Liu P. J. Ho, and J. H. Eberly, "Theories of photoelectron correlation in laser-driven multiple atomic ionization," *Rev. of Mod. Phys.* **84**, 1011 (2012).
6. R. Grobe, and J. H. Eberly, "Photoelectron Spectra for a Two-Electron System in a Strong Laser Field," *Phys. Rev. Lett.* **68**(19), 2905-2908. (1992).
7. R. Grobe, K. Wewskit, and J. H. Eberly, "Measure of electron-electron correlation in atomic physics," *J. Phys. B: At. Mol. Opt. Phys.* **27**, 503-508 (1994).
8. W.-C. Liu, J. H. Eberly, and S. L. Haan, "Correlation Effects in Two-Electron Model Atoms in Intense Laser Fields," *Phys. Rev. Lett.* **83**, 520, (1999).
9. K. Banaszek, and K. Wódkiewicz, "Testing Quantum Nonlocality in Phase Space," *Phys. Rev. Lett.* **82**(10), 2009 (1999).
10. K. Banaszek and K. Wódkiewicz, "Nonlocality of the Einstein-Podolsky-Rosen state in the Wigner representation," *Phys. Rev. A* **58**(6) (1998).
11. N. Suárez, A. Chacón, M. F. Ciappina, J. Biegert and M. Lewenstein, "Above-threshold ionization and photoelectron spectra in atomic systems driven by strong laser fields," *Phys. Rev. A* **92**, 063421 (2015).
12. N. Suárez, A. Chacón, M. F. Ciappina et al., "Above-threshold ionization and laser-induced electron diffraction in diatomic molecules," *Phys. Rev. A* **94**(4), 043423 (2016).
13. N. Suárez, A. Chacón, E. Pisanty, L. Ortmann, A. S. Landsman, A. Picón, J. Biegert, M. Lewenstein, and M. F. Ciappina, "Above-threshold ionization in multicenter molecules: The role of the initial state," *Phys. Rev. A* **97**, 033415 (2018).
14. N. Suárez, A. Chacón, J. A. Pérez-Hernández, J. Biegert, M. Lewenstein, and M. F. Ciappina, "High-order-harmonic generation in atomic and molecular systems," *Phys. Rev. A* **95**, 033415 (2017).
15. A. Galstyan, Y. V. Popov, F. Mota-Furtado et al., "Modelling laser-atom interactions in the strong field regime," *Eur. Phys. J. D* **71**(4), 97 (2017).
16. P. Agostini, F. Fabre, G. Mainfray, G. Petite and N. K. Rahman, "Free-free transitions following six-photon ionization of xenon atoms," *Phys. Rev. Lett.* **42**(17), 1127–1130 (1979).
17. M. D. Feit, J. A. Fleck and A. Steiger, "Solution of the Schrödinger Equation by a Spectral Method," *J. Comp. Phys.* **47**, 412-433 (1982).
18. M. Protopapas, D. G. Lappas and P. L. Knight, "Strong Field Ionization in Arbitrary Laser Polarizations," *Phys. Rev. Lett.* **79**(23), 4550 (1997).
19. G. M. Muslu and H. A. Erbay, "Higher-order split-step Fourier schemes for the generalized nonlinear Schrödinger equation," *Math. and Comput. Simulat.* **67**(6), 581-595 (2005).
20. "Modelling of Nonlinear Propagation in Waveguides" in A. V. Lavrinenko, J. Lægsgaard, N. Gregersen, F. Schmidt, T. Søndergaard, *Numerical Methods in Photonics* (CRC press, 2014), Chap. 5.
21. R. Achilles and A. Bonfiglioli, "The early proofs of the theorem of Campbell, Baker, Hausdorff, and Dynkin," *Arch. Hist. Exact Sci.* **66**(3), 295-358 (2012).
22. G. Strang, "On the Construction and Comparison of Difference Schemes," *SIAM J. Num. Anal.* **5**, 506-517 (1968).
23. A. Scrinzi, "Time-Dependent Schrödinger Equation" in T. Schultz and M. Vrakking (eds.), *Attosecond and XUV Physics: Ultrafast Dynamics and Spectroscopy* (Wiley, 2014), Chap. 8. doi:10.1002/9783527677689.ch8
24. P. Bader, S. Blanes, and F. Casas, "Solving the Schrödinger eigenvalue problem by the imaginary time propagation technique using splitting methods with complex coefficients," *J. Chem. Phys.* **139**, 124117 (2013).
25. M. M. Rahman, "Code for Quantum Simulation of Attosecond Physics", Zenodo, doi:10.5281/zenodo.3382240 (2019).
26. M. Lewenstein, K. C. Kulander, K. J. Schafer, and P. H. Bucksbaum, "Rings in above-threshold ionization: A quasiclassical analysis," *Phys. Rev. A* **51**(2), 1495-1507 (1995).

Appendix

In the appendix section A1, we provide the derivation of the ground state of the separable potential and in the section A2, we present a comparison of ground states of an inverse-square-root model and a Gaussian model.

A1.1 Derivation of ground state of the Separable potential

$$\begin{aligned}
 \hat{H} &= \frac{1}{2m} \hat{p}^2 + (-\gamma)|\phi\rangle\langle\phi| \\
 \Rightarrow \quad \langle p|\hat{H}|\psi_0\rangle &= \frac{1}{2m} p^2 \langle p|\psi_0\rangle + (-\gamma)\langle p|\phi\rangle\langle\phi|\psi_0\rangle
 \end{aligned}
 \quad \left| \quad \right.
 \quad \langle\phi|\psi_0\rangle = \int \frac{\langle\phi|p\rangle}{\phi^*(p)} \frac{\langle p|\psi_0\rangle}{\psi_0(p)} dp$$

$$\begin{aligned}
\Rightarrow \quad \frac{(-I_p) \langle p | \psi_0 \rangle}{\psi_0(p)} &= \frac{1}{2m} p^2 \frac{\langle p | \psi_0 \rangle}{\psi_0(p)} - \gamma \frac{\langle p | \phi \rangle}{\phi(p)} \langle \phi | \psi_0 \rangle \quad \left| \quad \right. &= \int \gamma \frac{\phi^*(p) \phi(p)}{I_p + \frac{1}{2m} p^2} \langle \phi | \psi_0 \rangle dp \\
\Rightarrow \quad \psi_0(p) &= \frac{\gamma \langle \phi | \psi_0 \rangle}{N} \frac{\phi(p)}{\frac{1}{2m} p^2 + I_p} \quad \left| \quad \right. &\Rightarrow \gamma = \left(\int \frac{|\phi(p)|^2}{I_p + \frac{1}{2m} p^2} dp \right)^{-1}
\end{aligned}$$

From the expressions we observe that both the ground state and the coupling constant depend on ionization potential.

A1.2 Derivation of adjusted ground state of the Separable potential

Inserting $e^{-i\hat{H}\Delta t} = e^{-i\frac{\hat{p}^2}{4}\Delta t} [\mathbb{I} + (e^{i\gamma\Delta t} - 1)|\phi\rangle\langle\phi|] e^{-i\frac{\hat{p}^2}{4}\Delta t}$ and $E = -I_p$ into $\langle p | e^{-i\hat{H}\Delta t} | \psi \rangle = \langle p | e^{-iE\Delta t} | \psi \rangle$ we obtain:

$$\begin{aligned}
e^{-i\frac{p^2}{4}\Delta t} \left[e^{-i\frac{p^2}{4}\Delta t} \psi(p) + (e^{i\gamma\Delta t} - 1) \phi(p) \left\langle \phi \left| e^{-i\frac{\hat{p}^2}{4}\Delta t} \psi \right\rangle \right] &= e^{iI_p\Delta t} \psi(p) \\
\Rightarrow \psi(p) &= \frac{N e^{+i\frac{p^2}{4}\Delta t}}{1 - e^{i(I_p + \frac{p^2}{2})\Delta t}} \phi(p), \quad \left| \quad \right. \quad \left\langle \phi \left| e^{-i\frac{\hat{p}^2}{4}\Delta t} \psi \right\rangle = \int \phi^*(p) e^{-i\frac{\hat{p}^2}{4}\Delta t} \psi(p) dp \right. \\
\text{where} & \quad \quad \quad = \int \frac{N |\phi(p)|^2}{1 - e^{i(I_p + \frac{p^2}{2})\Delta t}} dp \\
N &= (1 - e^{i\gamma\Delta t}) \left\langle \phi \left| e^{-i\frac{\hat{p}^2}{4}\Delta t} \psi \right\rangle \quad \quad \quad \Rightarrow \gamma = \frac{1}{\Delta t} \text{Im} \left[\ln \left(1 - \left[\int \frac{N |\phi(p)|^2}{1 - e^{i(I_p + \frac{p^2}{2})\Delta t}} dp \right]^{-1} \right) \right]
\end{aligned}$$

In this case, the ground state and the coupling constant are adjusted in accordance with the time-step used in the simulation. In the limit of very small time-step the expression of $\psi(p)$ in this section converges to the one derived in section A1.1.

A2 Comparison between two models of ground states

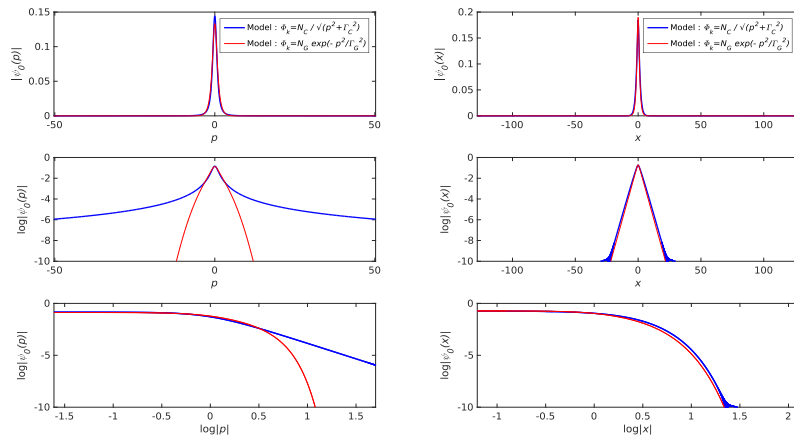


Fig. S1. In this figure, we compare the ground states of the separable potential for inverse-square-root model (in blue) and Gaussian model (in red) in both momentum space (left) and position space (right). In this simulation $\Gamma_c = 1$ and $I_G = 3$ are used.